www.nature.com/scientificreports

scientific reports

Analysis of the relationship between rod cell membrane currents and the photoreceptor component of electroretinograms using a cable model

Shaocong Ou[1], Kouta Hori[1], Yuttamol Muangkram[1], Yukiko Himeno[1], Shuji Tachibanaki[2] & Akira Amano[1]✉

This study presents a one-dimensional bidomain cable model for analyzing the relationship between rod membrane currents and rod electroretinogram (ERG) waveform components. The model incorporates the detailed structural and electrophysiological properties of rod photoreceptors by assuming the distribution of various ion currents. Simulation results indicate that the outer segment current (I_{photo}) primarily influences the photoreceptor component of ERG in low-intensity light, while the transient potential notch shape called "nose," observed under high-intensity light stimulation, is mainly attributed to the I_h current in the inner segment. In addition, capacitive currents in the outer segment play a crucial role in maintaining extracellular current loops when I_{photo} is inactive. These findings highlight that currents other than I_{photo}, such as I_h and capacitive currents, contribute significantly to the ERG waveform, particularly under high-intensity light, as theoretically suggested by Robson et al. The model successfully reproduced the experimentally measured rod ERG waveforms and their local components, providing a foundational platform for further investigation of ERG mechanisms. This enhanced understanding could lead to improved clinical applications of ERG in the diagnosis and assessment of retinal conditions. Future work will focus on refining the ion channel distribution, incorporating additional transport mechanisms, and validating the model using a broader range of experimental data to better replicate the complex electrophysiological phenomena of rod photoreceptor cells.

Keywords Electroretinogram, A-wave, Bidomain model, Mathematical model, Rod photoreceptor cell

The retina is the part of the eye that senses light and communicates this information to the brain via the optic nerve. Rod photoreceptors mediate night vision, whereas cone photoreceptors enable the observation of fine details and colors in daylight. Many retinal diseases leading to blindness are caused by photoreceptor dysfunction. An electroretinogram (ERG) is a complex field potential widely used to monitor retinal function and resolve the basic mechanisms of vision in the retina[1]. In recent years, expanding research on hereditary eye diseases and the development of transgenic animal models have led to a growing interest in the use of ERG[2–4]. Although ERG signals have long been characterized with regard to several components that vary according to their known cellular and molecular origins, the quantitative origins and characteristics of these components remain unresolved, limiting the application of ERG in the study of disease pathogenesis and treatment efficacy[4,5]. To facilitate effective and quantitative use of ERG, it is important to understand the origins of these signal components.

Photoreceptors contribute to ERG by generating the a-wave, a negative corneal potential that is the earliest event when a bright stimulus is applied[6–16]. Following the a-wave, a positive-going b-wave is generated by bipolar and/or Muller cells[17–19]. Other components, such as the c-wave, d-wave, and oscillatory potentials (OPs), are

[1]Graduate School of Life Sciences, Ritsumeikan University, Kusatsu City, Shiga, Japan. [2]Division of Biology, Department of Natural Science, The Jikei University School of Medicine, Tokyo, Japan. ✉email: a-amano@fc.ritsumei.ac.jp

associated with the retinal pigment epithelium (RPE), OFF-type bipolar cells, and middle retinal cells such as amacrine cells[6,20,21].

The a-wave finding is significant and considerably guides the differential diagnosis. In both genetic diseases (where the a-wave can narrow the list of genes likely to be associated with the disease) and acquired diseases, abnormalities in the a-wave can serve as practical indicators for diagnosing retinal disorders, such as congenital stationary night blindness, melanoma-associated retinopathy, and X-linked retinoschisis[22,23]. Similar to an electrocardiogram, ERG may provide a direct correlation between specific waveform changes and underlying pathological conditions, enabling precise diagnoses[24].

The a-wave analysis was initiated by Granit, who first separated the PI, PII, and PIII components, marking the beginning of research on ERG waveforms[6]. Later studies reported that the mathematical formula proposed by Lamb and Pugh provided a good approximation for explaining the leading edge of an a-wave[8–11]. In these studies, the a-wave, which is the PIII component of the ERG, was assumed to be identical to the outer segment current of the photoreceptors. This assumption provides a good approximation in low-intensity lighting conditions. However, experiments under high-intensity lighting conditions revealed the presence of the "nose" waveform, a steep positive potential following the initial negative signal in the a-wave, which is not observed in the outer segment current. This indicates that this assumption is not entirely correct[25–27].

The "nose" waveform has been reported to disappear when the I_h is blocked, suggesting that the I_h current is related to its origin[28,29]. However, whether I_h alone is responsible for the formation of the "nose" waveform is still debatable. This issue arises because the quantitative relationship between the ERG and photoreceptor ion currents has not been clearly defined. The photoreceptors that generate a-waves have long and narrow structures composed of an outer segment, inner segment, cell body, axon, and synaptic terminal[30]. Understanding the spatial distribution of ionic currents in these cells is essential to clarify the relationship between ionic currents and the mechanism of a-wave generation.

To address this problem, circuit models have been used to analyze the ERG waveform generation mechanism. Robson et al. used a current model primarily focusing on the outer segment current (I_photo), including the cyclic nucleotide-gated channel current (I_CNG) and potassium-gated sodium calcium exchanger current (I_NCKX), along with a simple passive circuit model with a capacitor representing the membrane capacitance, to analyze the relationship between the ERG waveform, outer segment current, and capacitive current[4,31,32]. They concluded that the capacitive current partially contributed to the ERG waveform. However, this model does not incorporate the physiological ion currents reported in photoreceptors other than the outer segment current, indicating that the relationship between photoreceptor ion currents, particularly I_h, and the ERG waveform has not been analyzed in detail.

Subsequent studies, such as those using circuit models by Tyler, did not implement the detailed ion currents present in the photoreceptors, and the relationship between the ERG waveform and ion currents has not been quantitatively analyzed[33]. Concerning the ion current models of photoreceptors, a salamander photoreceptor ion current model proposed by Kamiyama et al. has been introduced[34,35]. Several studies have reported ion currents present in photoreceptors; however, research on the localization of ion currents critical for ERG generation remains limited[31,36–44]. In most cases, studies have reported the localization of ion channel proteins through immunostaining techniques, but not current densities.

To fill this gap, this study aims to develop a new mathematical model that differs from the simplified circuit models. This model approaches the a-wave generation mechanism, which is an ERG characteristic, from the perspective of ionic currents, which is a cellular property. A one-dimensional (1D) bidomain cable model was developed to analyze the distribution of various ionic currents within the photoreceptors and their relationship with a-wave generation. Through this approach, we aim to overcome the limitations of the existing models, provide a new theoretical framework, and achieve a deeper understanding of the a-wave generation mechanism.

Methods

In this study, we hypothesized that the photoreceptor component of ERG waveforms could be explained by a 1D electrophysiological bidomain cable model of photoreceptor cells (Fig. 1).

Single-cell model

In this section, we describe the single-cell model used to construct the 1D cable model. Because this study aimed to construct an ERG analysis platform for clinical examinations, the single-cell model needed to be based on at least mammalian cells. However, to date, no detailed mammalian photoreceptor electrophysiological models have been proposed. The most widely used model in which the electrophysiological properties have sufficient accuracy is the one proposed by Kamiyama et al.[34,35]. , which was constructed using data from lower vertebrates and incorporates the newt photosensitive current model. Thus, we used this model with modifications to the photosensitive current model to reproduce the shorter reaction times observed in mammalian data[14].

In the Kamiyama model, the outer segment current is called I_photo, based on the Newt model proposed by Torre et al.[45]. Although the Torre model provides a good representation of I_photo from newts and other amphibians, the mammalian I_photo is shorter than that of newts. Pahlberg et al.[14]. have reported that a typical mouse I_photo for rods has a duration of 0.5–2.0 s, while that of a newt ranges from 2.0 to 6 s.

Abtout et al.[46]. proposed a mouse I_CNG model, which represents an actual photosensitive current carried by a cyclic nucleotide-gated (CNG) channel. Therefore, we used the Abtout model as the basis for our I_photo to achieve a better I_photo time course of mouse data[14]. The pigment molecule reactions are activated by a light stimulus (Rh*) and activated transducin (Tr*). Light-activated phosphodiesterase (PDE*) was used in the proposed model, whereas the equations of the Kamiyama model were used for the time course of cyclic guanosine monophosphate (cGMP)-dependent I_photo, which is the summation of I_CNG and the potassium-dependent sodium–calcium

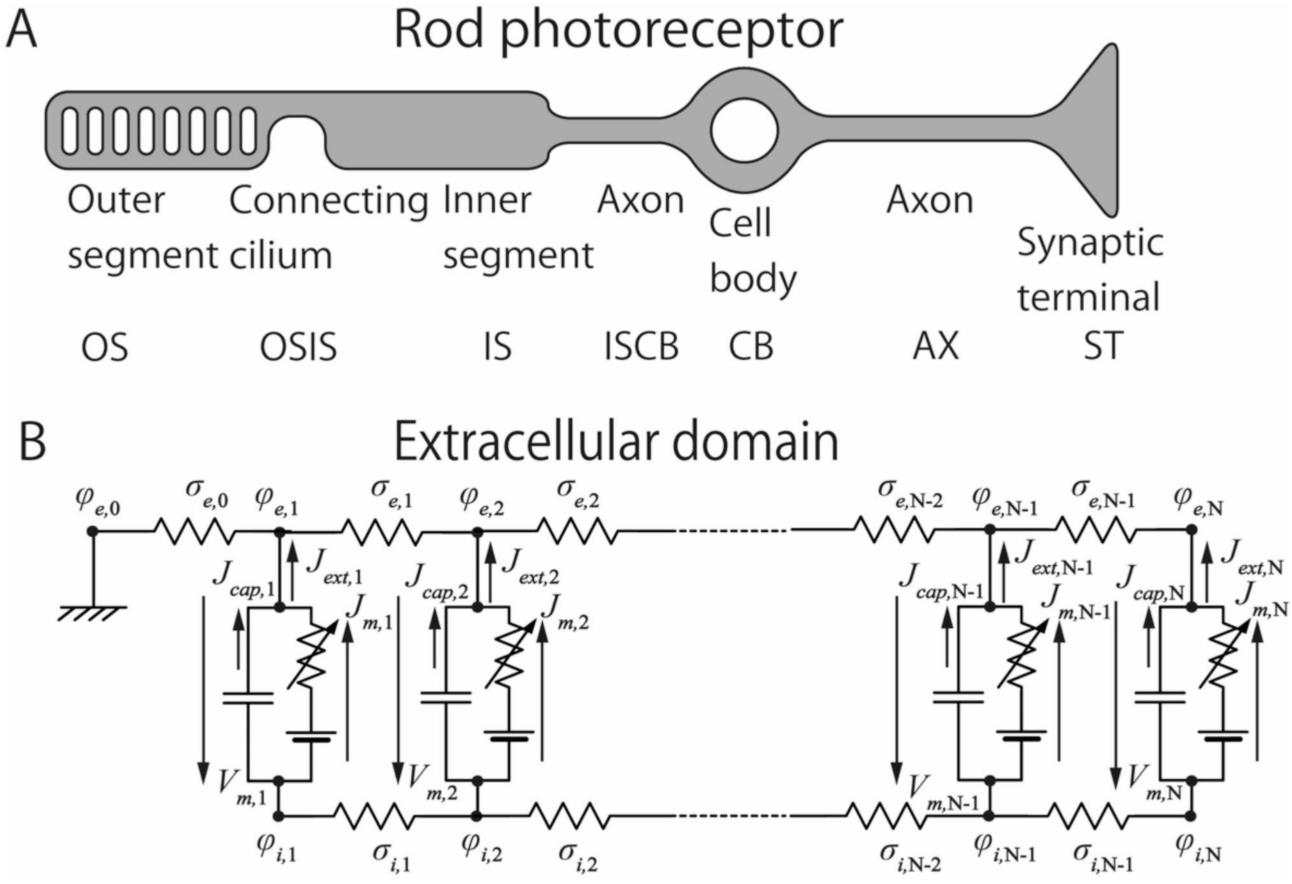

Fig. 1. The proposed photoreceptor cell model and its circuit model. (**A**) The proposed photoreceptor cell model; (**B**) A 1D bidomain model. The upper edge of B represents the extracellular domain, and the lower edge, the intracellular domain. $\sigma_{e,\,k}$, extracellular conductivity; $\varphi_{e,\,k}$, extracellular potential; $\sigma_{i,\,k}$, intracellular conductivity; $\varphi_{i,\,k}$, intracellular potential; $J_{cap,\,k}$, capacitive current per unit volume; $J_{m,\,k}$, membrane current per unit volume; $J_{ext,\,k}$, extrusive current per unit volume; N, number of lattice points; $V_{m,\,k}$, membrane potential.

exchanger current, I_{NCKX}. Therefore, other ion channel and transporter model equations, including those for I_h, I_{Kv}, I_{Ca}, $I_{Cl(Ca)}$, $I_{K(Ca)}$, I_{leak}, I_{NCX}, and I_{PMCA}, were incorporated into the Kamiyama model[34,35].

Several processes contribute to neuronal calcium dynamics[47]. Once calcium ions enter a cell through calcium channels, they diffuse and bind to various buffers. Because the intracellular mechanisms that regulate intracellular calcium ions are not fully understood, calcium systems were modeled using minimal mechanisms to reproduce calcium-dependent currents in a single-cell model[45,48].

The intracellular Ca^{2+} mechanism in the single-cell model is the same as that in the Kamiyama model[34,35]. Intracellular calcium is divided into two areas of the cell: the space immediately below the plasma membrane ($[Ca^{2+}]_s$) and the central space ($[Ca^{2+}]_f$). This allows for the regulation of intracellular calcium by facilitating influx via I_{Ca}, extrusion via transporters, and both binding to and separation from internal buffers with high affinity ($[Ca^{2+}]_{hs}$ and $[Ca^{2+}]_{hf}$) and low affinity ($[Ca^{2+}]_{ls}$ and $[Ca^{2+}]_{lf}$), respectively.

In the subsequent section, we elaborate on the transformation of a single-cell model into a 1D cable model. Our exposition will encompass the meticulous elucidation of six fundamental facets: model structure, electrical circuit model, intracellular and extracellular conductance, membrane capacitance, ion current distribution, and calcium ion diffusion.

1D cable model

Model structure

A 1D cable model was constructed to incorporate the structural compartments of photoreceptor cells. These are the outer segment (OS), connecting cilium (OSIS), inner segment (IS), myoid connecting the inner segment and cell body (ISCB), cell body (CB), axons connecting the cell body and synaptic terminal (AX), and synaptic terminal (ST) (Fig. 1A).

The size of photoreceptor cells, their cross-sectional areas, and the length of each structural compartment vary between species and, to a lesser extent, between cells within the same retina. In our model, reported values obtained from published information on the photoreceptors of humans and mice were used for the lengths (Table 1)[49–52].

Com	Diameter (μm)	Ref	Length (μm)	Ref
OS	2.09	[51]	29.41	[49]
OSIS	0.45	[52]	0.70	[49]
IS	1.95	[51]	26.9	[49]
ISCB	0.45	[52]	19.08	[49]
CB	4.58	[49]	6.96	[49]
AX	0.45	[52]	26.98	[49]
ST	3.0	[50]	1.867	[50]

Table 1. The diameter and length of each cell compartment in the proposed rod photoreceptor cell model. *OS* outer segment, *OSIS* cilium, *IS* inner segment, *ISCB* myoid connecting the inner segment and the cell body, *CB* cell body, *AX* axon connecting the cell body and the synaptic terminal, *ST* synaptic terminal, *Com* compartment, *Ref* reference.

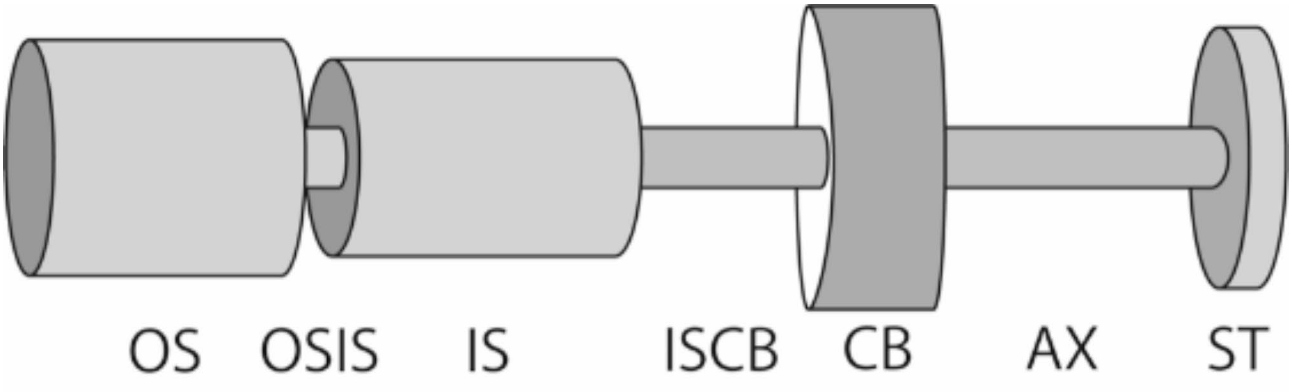

Fig. 2. A rod photoreceptor cell represented by combining multiple cylinders.

The compartments of rod photoreceptor cells have different diameters. To reflect this difference in our model, we divided it into seven compartments (OS, OSIS, IS, ISCB, CB, AX, and ST), and used a cylinder to represent each compartment, as shown in Fig. 2. These cylinders were connected in an appropriate sequence to create the 3D structure and shape of the entire rod photoreceptor cell.

Utilizing the length data of the rod cells, as shown in Table 1, our approach involved segmenting the 1D cable model into 100 equidistant intervals. Individually corresponding to the length of each compartment facilitates the determination of the segmentation points within the rod photoreceptor cell model. Specifically, segments 1–26 delineate the OS, whereas segment 27 denotes the OSIS. Segments 28–51 encapsulate the IS, with segments 52–68 representing the ISCB. Segments 69–74 are attributed to the CB, followed by segments 75–98, corresponding to the AX. Finally, segments 99–100 signify ST.

Electrical circuit model

To calculate the extracellular potential, a bidomain model was used to represent the cable model (Fig. 1B). The cable was represented by N lattice points with one extracellular point outside the cell, with intervals Δ_x in the longitudinal direction. Intracellular current ($J_{i,\,k}$), extracellular current ($J_{e,\,k}$), capacitive current ($J_{cap,\,k}$), membrane current ($J_{m,\,k}$), intracellular conductivity ($\sigma_{i,\,k}$), extracellular conductivity ($\sigma_{e,\,k}$), and extrusive current ($J_{ext,\,k}$) were included in the model.

Intracellular and extracellular conductance

Various values of intracellular (R_i) and extracellular conductance (R_e) were used in the biological bidomain equation because a clear agreement on the appropriate values is lacking[53]. We used typical conductivity values reported by Hagins et al.[54]. The intra- and extracellular conductances of the cells in different compartments were calculated based on the cross-sectional area of the defined unit segments. Conductance was calculated using the available physiological measurement data for the intracellular space within the unit segment. However, detailed physiological data are not available for extracellular conductance. Therefore, we conducted extensive measurements of the extracellular space surrounding the rod photoreceptor cells using low-magnification electron micrographs of the longitudinal section of the entire photoreceptor layer[55]. The average value obtained from these measurements was used to calculate the conductance of the extracellular space within the unit segments.

Membrane capacitance

According to the Kamiyama model[34,35], the total membrane capacitance of a single-rod photoreceptor in vertebrates (C_m) is 20 nF, which has a scale of approximately 0.2383 relative to that of mice provided by Hagins et al.[54]. Therefore, in this model, the membrane capacitance was derived by applying this scale to the values, and the membrane capacitance at each lattice point was obtained from the ratio of the surface area of each compartment. Simultaneously, all ion–current conductances in the proposed model were adjusted using this ratio. The surface area of each compartment was calculated using Eq. (1), where D_C and L_C represent the diameter and length of compartment C, respectively.

$$s_a = \pi D_c L_c, \ (C \in X) \tag{1}$$

where

$$X \in \{OS, \ OSIS, \ IS, \ ISCB, \ CB, \ AX, \ ST\}. \tag{2}$$

Ion current distribution

It is known that only I_{photo} exists in the OS, which includes I_{CNG} and I_{NCKX}[34,35]. We assumed that all cell compartments other than the OS had I_{leak}. For all other currents, we referred to immunostaining studies to determine which ion channels (or transporters) were localized in which compartments.

I_{h} was present in the IS and ST of rod photoreceptor cells in mice according to the immunostaining results of Fortenbach et al.[44].

For I_{Kv}, immunostaining by Jiang et al.[31]. confirmed that Kv2.1 is present in the IS, and Kv8.2 in the IS and ST of mouse rod photoreceptor cells.

For I_{Ca}, immunostaining by Knoflach et al.[41]. confirmed that Cav1.4 is localized in the ST of rod photoreceptor cells in mice.

For $I_{\text{Cl(Ca)}}$, ANO1 (TMEM16A) was confirmed to be localized in the ST by Caputo et al.[43]. and Jeon et al.[42]. Stohr et al.[39]. confirmed that ANO2 (TMEM16B) is localized in the IS and ST of rod photoreceptor cells in mice.

For I_{NCX}, immunostaining performed by Kizhatil et al.[38]. revealed that NCX1 was localized in the IS and ST of rod photoreceptor cells in mice.

For I_{PMCA}, Morgans et al.[36]. confirmed that PMCA transporters are localized in the IS and ST of rod photoreceptor cells in rats.

Tanimoto et al.[40]. failed to confirm the presence of $I_{\text{K(Ca)}}$ in mice. However, it exhibits gene expression in the mouse retina[56]. Therefore, we assumed that all cell compartments, other than the OS and OSIS, contained $I_{\text{K(Ca)}}$.

Table 2 lists the compartments in which the ion currents were implemented in our model. The cilium (OSIS) is very short; therefore, only a I_{leak} channel was implemented.

The channel conductance of each ion current at each lattice point varies depending on the cell compartment in which it is present. I_{h} and I_{Kv} are mainly concentrated in the IS; we assumed that 90% of the conductance of these two ion currents is in the IS, and the remaining 10% was determined by the ratio of the surface areas of the compartments using Eq. (1). I_{Ca} and $I_{\text{Cl(Ca)}}$ are primarily located in the ST, and we assumed that 95% and 49% of the conductance of these two ion currents are in the ST, respectively, and the remaining 5% and 51% were determined by the ratio of the surface areas of the compartments except the ST using Eq. (1)[57]. The conductance distribution for I_{NCX} and I_{PMCA} was adjusted based on the data reported by Johnson et al.[55]. Finally, the conductance distributions of $I_{\text{K(Ca)}}$ and I_{leak} were determined from the ratio of the surface areas of the compartments using Eq. (1).

Ref	Channel	Compartment						
		OS	OSIS	IS	ISCB	CB	AX	ST
35	I_{photo}	+	–	–	–	–	–	–
41	I_{Ca}	–	–	+	+	+	+	+
39,42,43	$I_{\text{Cl(Ca)}}$	–	–	+	+	+	+	+
38	I_{NCX}	–	–	+	+	+	+	+
36	I_{PMCA}	–	–	+	+	+	+	+
40	$I_{\text{K(Ca)}}$	–	–	+	+	+	+	+
31	I_{Kv}	–	–	+	+	+	+	+
44	I_{h}	–	–	+	+	+	+	+
35	I_{leak}	–	+	+	+	+	+	+

Table 2. Ion channel distribution of our proposed model of a rod photoreceptor cell. The (+) indicates that the ion channel was implemented in the compartment, and the (–) indicates that it was not implemented. *AX* axon connecting the cell body and the synaptic terminal, *CB* cell body, *IS* inner segment, *ISCB* myoid connecting the inner segment and the cell body, *OS* outer segment, *OSIS* cilium, *ST* synaptic terminal, *Ref* reference.

Calcium ion diffusion

Because each lattice point had calcium ion (Ca^{2+}) diffusion compartments, Ca^{2+} diffusion between adjacent lattice points was added to the cable model. The intracellular Ca^{2+} dynamics of the outer and inner segments in the proposed model are shown in Fig. 3.

There were three types of Ca^{2+} concentrations in the proposed model: $[Ca^{2+}]_{OS}$ in the OS, where I_{photo} was implemented; $[Ca^{2+}]_s$ between the OSIS and ST, which is the Ca^{2+} concentration near the cell membrane; and $[Ca^{2+}]_f$ between the OSIS and ST, which is the Ca^{2+} concentration deep in the cytoplasm. Regarding the diffusion of Ca^{2+} between each compartment, we assumed that Ca^{2+} diffusion may occur between $[Ca^{2+}]_{OS}$ in the OS and $[Ca^{2+}]_s$ in the IS, $[Ca^{2+}]_s$ in the IS, $[Ca^{2+}]_s$ in the CB, $[Ca^{2+}]_f$ in the IS, $[Ca^{2+}]_f$ in the CB, and $[Ca^{2+}]_s$ and $[Ca^{2+}]_f$ in the IS and CB.

Note that a buffer called calbindin (Cab) is bound to $[Ca^{2+}]_{OS}$ in the OS and was included in the I_{photo} model.

Fick's first law equation was used to calculate Ca^{2+} diffusion between lattice points. F_k was calculated using the following equation from Fick's equation:

$$F_k = B_k d_{Ca} \frac{\left[Ca^{2+}\right]_k - \left[Ca^{2+}\right]_{k+1}}{\Delta_x} \tag{3}$$

where d_{ca} ($\mu m^2/s$) is the Ca^{2+} diffusion coefficient; $[Ca^{2+}]_k$ and $[Ca^{2+}]_{k+1}$ ($\mu mol/m^3$) are the Ca^{2+} concentrations at points k and $k+1$, respectively; x (μm) is the spatial direction; Δ_x (μm) is the interval between two lattice points; B_k (μm^2) is the cross-sectional area at k; and F_k (μmol/s) is the flux through lattice points k and $k+1$.

$[Ca^{2+}]_{s,k}$ is the calcium concentration at the k-th lattice point near the cell membrane between the OSIS and ST, and $[Ca^{2+}]_{f,k}$ is the calcium concentration at the k-th lattice point deep in the cell between the OSIS and ST. Note that because $[Ca^{2+}]_{OS}$ is the calcium concentration involved in I_{photo}, it was assumed that diffusion occurs between $[Ca^{2+}]_s$ in the vicinity of the cell membrane. Denoting the name of the compartment at lattice point k as C_k, the cross-sectional area at lattice point k was determined using Eq. (4). Smaller values of $B_{i,k}$ and $B_{i,k+1}$ were used for the cross-section B_k.

$$B_{s,k} = \pi \left(\frac{D_{C_k}}{2}\right)^2 \tag{4}$$

By representing the cell volume at lattice point k as s_k, the changes in Ca^{2+} at the k-th lattice point were calculated using the following equation:

$$\frac{d\left[Ca^{2+}\right]_k}{dt} = \frac{F_{k-1} - F_k}{s_k} \tag{5}$$

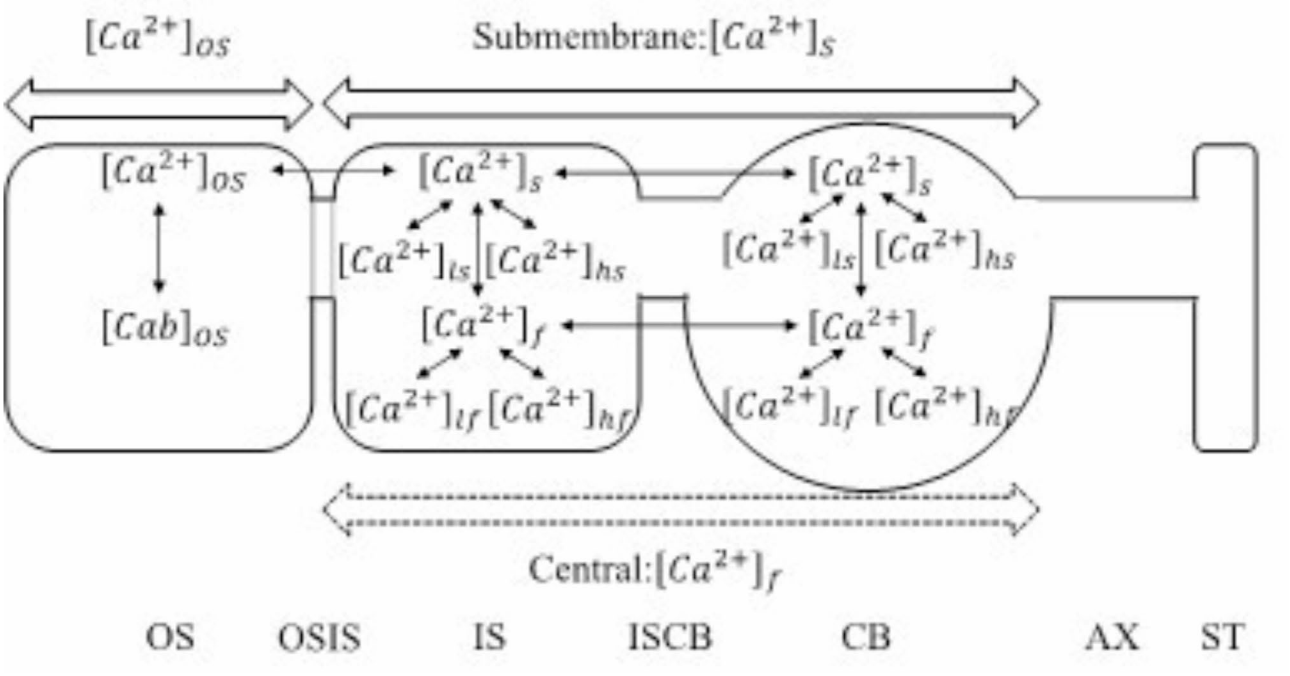

Fig. 3. Ca^{2+} system of the proposed rod photoreceptor cell model and the diffusion of Ca^{2+} between lattice points. *AX* axon connecting the cell body and the synaptic terminal, *CB* cell body, *IS* inner segment, *ISCB* myoid connecting the inner segment and the cell body, *OS* outer segment, *OSIS* ciliumm, *ST* synaptic terminal.

The diffusion fluxes $F_{s,k}$ near the plasma membrane and $F_{f,k}$ deep in the cytoplasm of the *k*-th Ca^{2+} ion between the OSIS and ST were calculated using $[Ca^{2+}]_s$ and $[Ca^{2+}]_f$, respectively.

Calculation scheme

In the bidomain model, the mesh spacing must be very small to reflect the anatomical and physiological results in sufficient detail. However, this method has a high computational cost[58–61]. Therefore, a numerical method that considers both the speed of the bidomain model and the accuracy of the numerical results is required. To achieve this, a solution coupled with the semi-implicit time-stepping method was used to compute the bidomain equations[62].

Results

Characteristics of the single-cell model

We first confirmed the behavior of the proposed single-cell model, which mimicked the characteristics of mouse rod photoreceptor cells (Fig. 4). Using the proposed single-cell model, we performed an ERG generation test with light stimulation at 10, 100, and 1000 Rh*/s intensities for 20 ms (Fig. 4).

First, in the dark condition, the membrane potential was in a state of equilibrium at about – 36 mV. After light stimulation, the membrane potential decreased further with increasing light intensity and then returned to the level observed in the dark (Fig. 4A).

The changes in the ion currents of I_{photo}, I_h, I_{Kv}, I_{Ca}, $I_{Cl(Ca)}$, $I_{K(Ca)}$, I_{leak}, I_{NCX}, and I_{PMCA} are shown in Fig. 4B-J. It can be seen that I_{photo}, I_{Kv}, I_{Ca}, $I_{K(Ca)}$, I_{leak}, and I_{PMCA} decreased with increased light intensity before recovering to the dark equilibrium. In contrast, I_h increased in response to increased light intensity before returning to dark equilibrium.

The $I_{Cl(Ca)}$ and I_{NCX} ion channels responded to increased light intensity by reaching a peak (higher with increasing intensity) and then decreased further with increasing intensity to an amplitude lower than the state of equilibrium before recovering to the dark equilibrium level.

Because our model was based on that of Kamiyama et al., its basic characteristics were very similar to those of the Kamiyama model[35,36]. However, the duration of each transient current flow was shorter, and the time course of I_{photo} was similar to that obtained from a mouse photoreceptor[14].

Reproduction of the ERG photoreceptor component

Figure 5 shows the electrophysiological characteristics of the rod photoreceptor cells under dark conditions and with a light stimulus. In Fig. 5A, the interstitial potential gradient along the length of the rat rod cell in

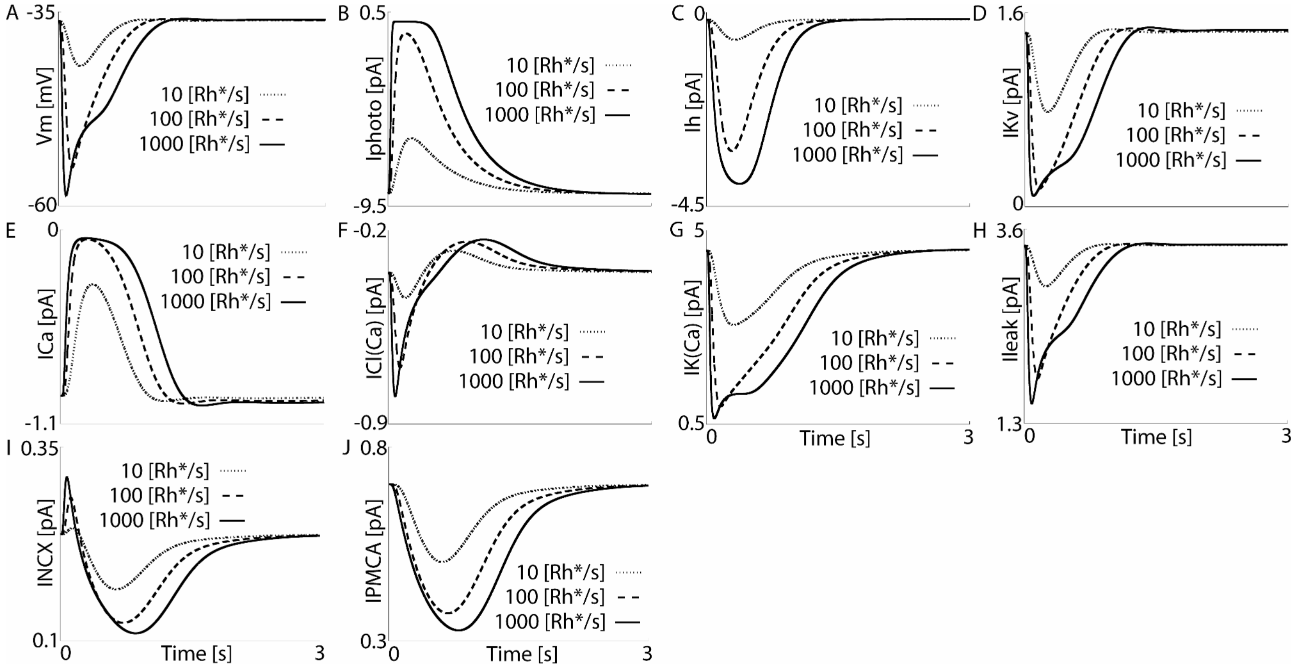

Fig. 4. Membrane potential and membrane ion currents of the proposed single-cell model of a mouse rod photoreceptor cell responding to light stimuli of different intensities. The dotted line represents a stimulus light intensity of 10 Rh*/s; the dashed line, a stimulus light intensity of 100 Rh*/s; and the solid line, a stimulus light intensity of 1,000 Rh*/s. The horizontal axis represents time (s), the vertical axis of (**A**) represents the membrane potential (mV), while the vertical axes of (**B–J**) represent the current (pA) of each ion channel. (**A**) depicts the membrane potential, (**B**) the I_{photo} current, (**C**) the I_h current, (**D**) the I_{Kv} current, (**E**) the I_{Ca} current, (**F**) the $I_{Cl(Ca)}$ current, (**G**) the $I_{K(Ca)}$ current, (**H**) the I_{leak} current, (**I**) the I_{NCX} current, and (**J**) the I_{PMCA} current.

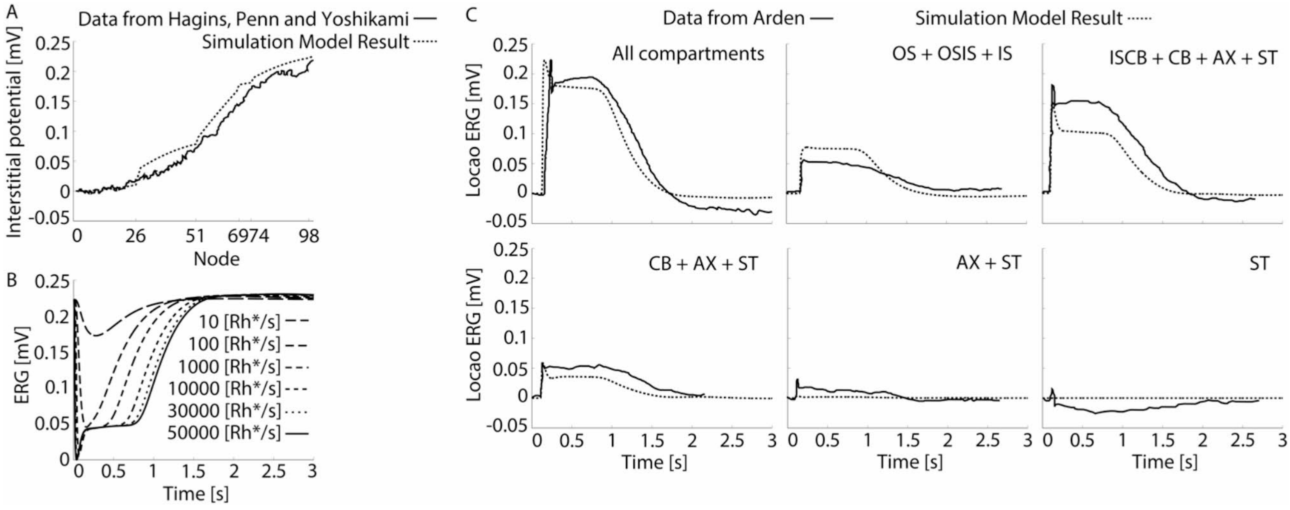

Fig. 5. Reported electrophysiological responses and results from the proposed computational model. (**A**) Interstitial potential data (solid line) across radial depth from the studies by Hagins, Penn, and Yoshikami[54], with the proposed model result (dotted line). (**B**) The electroretinogram (ERG) response of the proposed model to different intensities of light stimulus, measured in Rhodopsin molecules per second (Rh*/s). (**C**) Local ERG data (solid line) from the study by Arden[63], compared with corresponding local regional potential of the model (dotted line).

the dark state is shown as a solid line; the horizontal axis represents the lattice points, that is, the positions of the compartments of the proposed model; the vertical axis represents the interstitial potential. The simulation model results (dotted line) showed a high degree of accuracy with the experimental data of Hagins, Penn, and Yoshikami[54], suggesting a fair reproduction of cellular electrical activity. They conducted dark-adapted experiments for at least 10 min before being subjected to light pulses.

The proposed model was used to reproduce the photoreceptor component of the ERG waveforms with 20 ms of light stimulation at intensities of 10, 100, 1,000, 10,000, 30,000, and 50,000 Rh*/s under dark-adapted conditions. The resulting ERG waveforms (Fig. 5B) quantify the ERG response to light stimuli of different intensities, demonstrating the cell's graded response to increasing photon capture, as reflected by the ascending concentrations of rhodopsin activation. Pahlberg et al. reported transretinal ERG waveforms in mice lacking cone phototransduction that were administered aspartate to block the activity of bipolar cells[14]. The waveforms depicted in Fig. 5B show time courses and shapes similar to those reported by Pahlberg et al.[14]. When the intensity of the light stimulation was weak, the shape of the ERG was similar to that of I_{photo}. However, when the intensity of the light stimulation reached a certain level (estimated to be between 100 and 1000 Rh*/s), the shape of the ERG was significantly different from that of I_{photo}. The stronger the intensity of the light stimulation, the steeper the declining edge of the ERG. The simulation results were consistent with the experimental results of Robson[32].

Figure 5C further dissects the local ERG responses derived from Arden[63], broken down into different compartments of the rod photoreceptor cell, such as from the OS to the IS, from the ISCB to the ST, and others. Compared with the experimental data, the results of our simulation model with 20 ms of light stimulation at intensities of 30,000 Rh*/s under dark adaptation conditions showed that the local ERG of the entire model was fairly reproduced, and the local ERG between the OS and IS was higher. In addition, the local ERG between the ISCB and ST, CB and ST, and AX and ST was lower. The local ERG of the ST simulation model is also higher than that of the experimental data.

From the proposed simulation model, the local ERG between the OS and IS did not produce a "nose," and its shape was similar to that of the I_{photo}. In addition, the local ERG between the ISCB and ST showed an obvious "nose." This phenomenon is very similar to the experimental results of Arden[63] and confirms that "nose" formation is mainly related to the outer nuclear layer (ONL).

Although there were some differences between the experimental data and the simulation model results, this stratified representation provides insight into the localized variations in phototransduction efficiency and kinetics, revealing how each segment contributes distinctly to the overall photoreceptor response.

Origin of the ERG waveform

To understand the mechanism of ERG waveform generation, we used a high-light intensity condition, which produces a "nose" on the ERG waveforms. Under these conditions, the distributions of the extracellular potential, extracellular current, membrane potential, total ion current, and extrusive current at five different time points t_1–t_5 (Fig. 6A) were obtained, as shown in Fig. 6B–F, respectively. The membrane currents, including ion currents and extrusive currents shown in Fig. 6E,I, are the currents of each compartment; hence, the corresponding total cellular currents are the summation of all compartments that are confirmed to be close to the values shown in Fig. 4. Additionally, this is the same as in Figs. 7B,F, 8B,E and 10D, and 10F, and the capacitive currents in

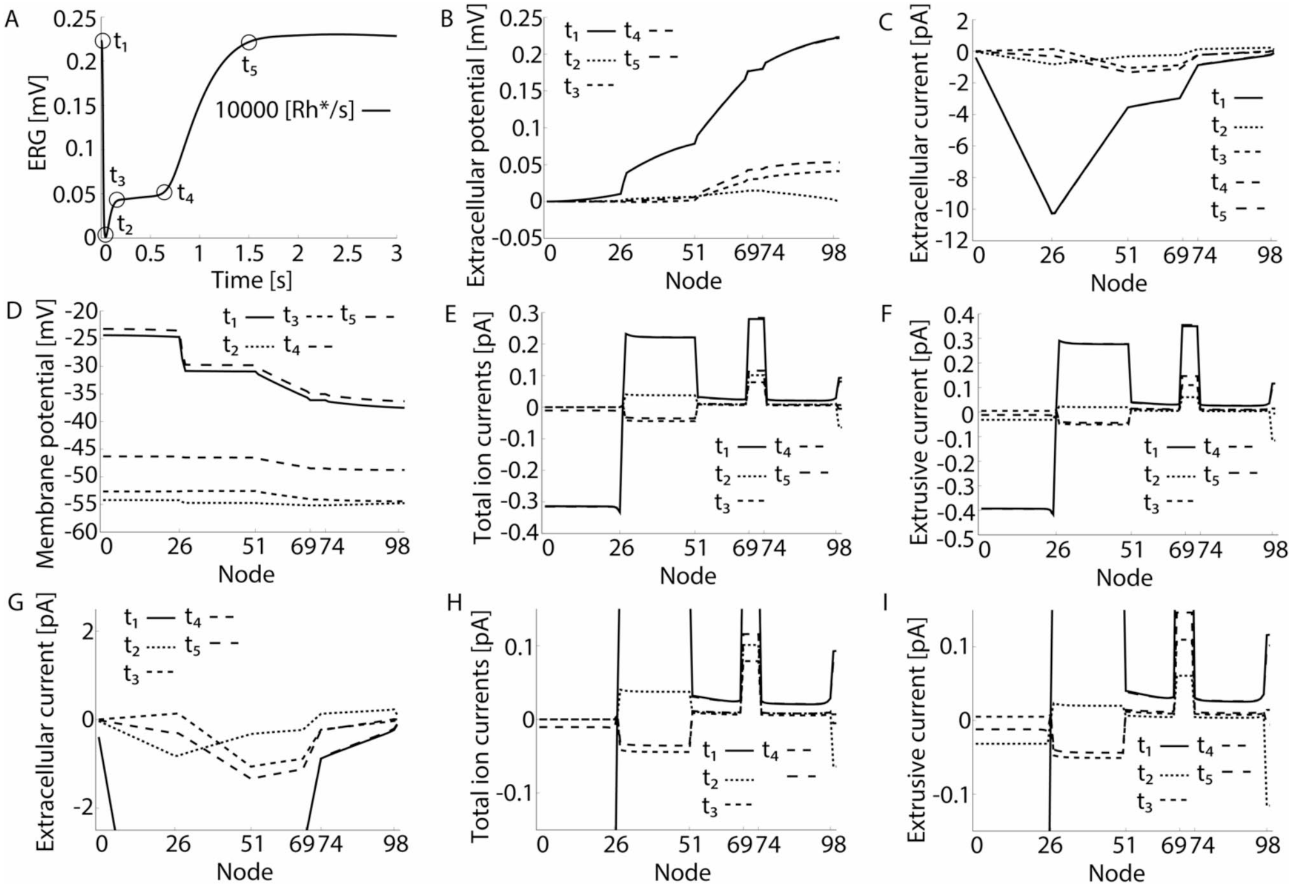

Fig. 6. Dynamic changes in rod photoreceptor cell electrophysiology over time and across cell compartments. (**A**) Time-course of the electroretinogram (ERG) amplitude with a high intensity light stimulus (10,000 Rh*/s). (**B**–**F**) Extracellular potential, extracellular currents, membrane potential, total ion currents, and extrusive currents, respectively, at different time points (t_1 through t_5 in (**A**)) across the rod photoreceptor's node. (**G**–**I**) Enlarged diagram of the extracellular currents (**C**), total ion currents (**E**), and extrusive currents (**F**).

Fig. 10E. The t_1 results in Fig. 6C show that in the dark state, the extracellular current outside the inner segment region is higher than that of other compartments, which is consistent with Arden's perspective[63].

When the rod photoreceptor cells were in the dark state (t_1 in Fig. 6A), the ERG potential was formed based on the extracellular potential difference between the OS and ST. The extracellular potential at the OS was lower than that at the ST (Fig. 6B), thus, an extracellular current was formed from the ST to OS, and the amplitude of the extracellular current increased from the ST to the IS and decreased from the IS to the OS (Fig. 6C,G). In addition, regardless of the total ion current ($J_{\mathrm{m,\,k}}$ in Figs. 1B and 6E) or extrusive current ($J_{\mathrm{ext,\,k}}$ in Figs. 1B and 6F), the OS was the sink of the extracellular current, and the others were the sources of the extracellular current. The membrane potential was between − 35 mV and − 25 mV.

When the rod photoreceptor cells were stimulated with light, the ERG amplitude decreased to a minimum value (t_2 in Fig. 6A). This is because the extracellular current flow decreased and the flow separated into two loops (Fig. 6C). One was formed from the CB to the OS, and the other was formed from the CB to the ST (Fig. 6G). The total ion currents were outward in the IS and CB, and inward in the ST (Fig. 6H). The extrusive current had traces of outward current in the CB and IS and inward current in the OS and ST (Fig. 6I). The difference between the total ion current and the extrusive current in the OS originates from the capacitive current. The membrane potential decreased to − 55 mV.

During the recovery to the dark state after the rod photoreceptor cells were stimulated by light, the potential difference between the OS and ST was slightly restored in the "nose" generation stage on the ERG waveform (t_3 in Fig. 6A). It should be noted that this is no longer the case in the previous current circuit. The extracellular current increases around the CB owing to the outward current in the CB. The total ion current, in the form of an inward current in the IS, results in a decrease in the extracellular current. The extracellular current in the direction of the IS generated in the OS flows into the cell at the IS. Because the total ion current is not generated in the OS (Fig. 6E,H), this current is completely discharged according to the extrusive current caused by the cell capacitance, which can be confirmed by the difference between the total ion current and the extrusive current (Fig. 6E,F,H,I). Thus, there is an inward current in the IS and ST, and an outward current in the OS and CB, forming one extracellular current circuit from the ST to the IS and another extracellular current circuit from the

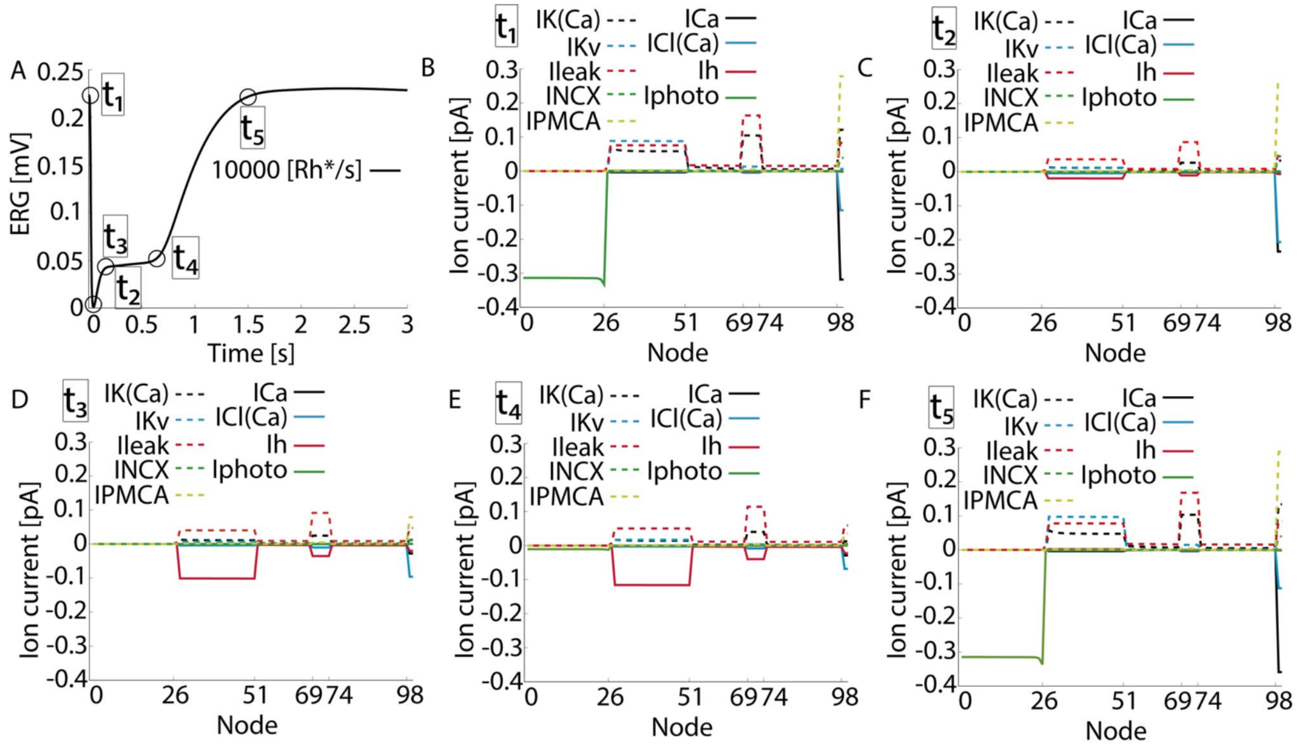

Fig. 7. Analysis of ionic currents in rod photoreceptor cells under high-intensity light stimulation. (**A**) Electroretinogram (ERG) response over time to a light stimulus of 10,000 Rh*/s. (**B**–**F**) Detailed profiles of individual ionic current components such as $I_{K(Ca)}$ (black dashed line), I_{Ca} (black solid line), I_{Kv} (light blue dashed line), $I_{Cl(Ca)}$ (light blue solid line), I_{leak} (red dashed line), I_h (red solid line), I_{NCX} (green dashed line), I_{photo} (green solid line), and I_{PMCA} (yellow dashed line), at specified time points (t_1 through t_5).

OS to the IS. This phenomenon was theoretically predicted by Robson et al.[32]. However, the rod cell membrane potential did not change significantly.

In addition, during recovery to the dark state, in the end stage of the "nose" on the ERG waveform (t_4 in Fig. 6A), the potential difference between the OS and ST did not change much compared with the generation stage of the "nose". The extracellular current flow was not large and only an extracellular current circuit was formed from the ST to the IS around the cell. At this time, the extracellular current increased because of the outward current flowing from the CB, and the inward current flowing through the OS and IS led to a decrease in the extracellular current. The reason for this change was that there was a small amount of inward current in the total ion current in the OS, and there was no obvious extrusive current in the OS. The membrane potential slightly increased to − 46 mV.

When the rod photoreceptor cells returned to the dark state after stimulation with light (t_5 in Fig. 6A), the extracellular potential distribution completely recovered to the same shape. The extracellular current, membrane potential, total ion current, and extrusive current almost completely returned to their spatial distributions under dark conditions.

Individual ion current composition of photoreceptor membrane currents

To analyze the relationships between the ERG waveform and individual ion currents in each compartment, we further analyzed the components of the membrane current shown in Fig. 6E at the five different time points shown in Fig. 7A, which are the same as those in Fig. 6A.

In the dark state (t_1 in Fig. 7A), the larger ion currents in each compartment were I_{photo} in the OS; I_{Kv}, $I_{K(Ca)}$ and I_{leak} in the IS; $I_{K(Ca)}$ and I_{leak} in the CB; and I_{PMCA} and I_{Ca} in the ST (Fig. 7B).

When the rod photoreceptor cell model received light stimulation and the ERG waveform dropped to the minimum value (t_2 in Fig. 7A), there was no ionic channel current in the OS (Fig. 7C). However, a capacitive current persisted in the OS, enabling the maintenance of the extracellular current loop from the CB to the OS. Although this capacitive current is not shown in Fig. 7 for simplicity, its presence is critical for sustaining the extracellular current loop observed in Fig. 6G even as the extracellular potential difference between the OS and ST approaches zero. Meanwhile, most ion channel currents in the other compartments decreased to levels close to zero. The most apparent change was the significant reduction in the $I_{K(Ca)}$ of the IS, and the CB and I_{Kv} of the IS. However, although I_{leak} also reduced, some of its current remained at the IS, CB, and ST. Similarly, large amounts of I_{PMCA}, I_{Ca}, and $I_{Cl(Ca)}$ remained in the ST, but the outward and inward currents were almost the same, resulting in a negligible extracellular current. It can be noted that in the process of decreasing almost all ion currents, I_h of the IS increases slightly.

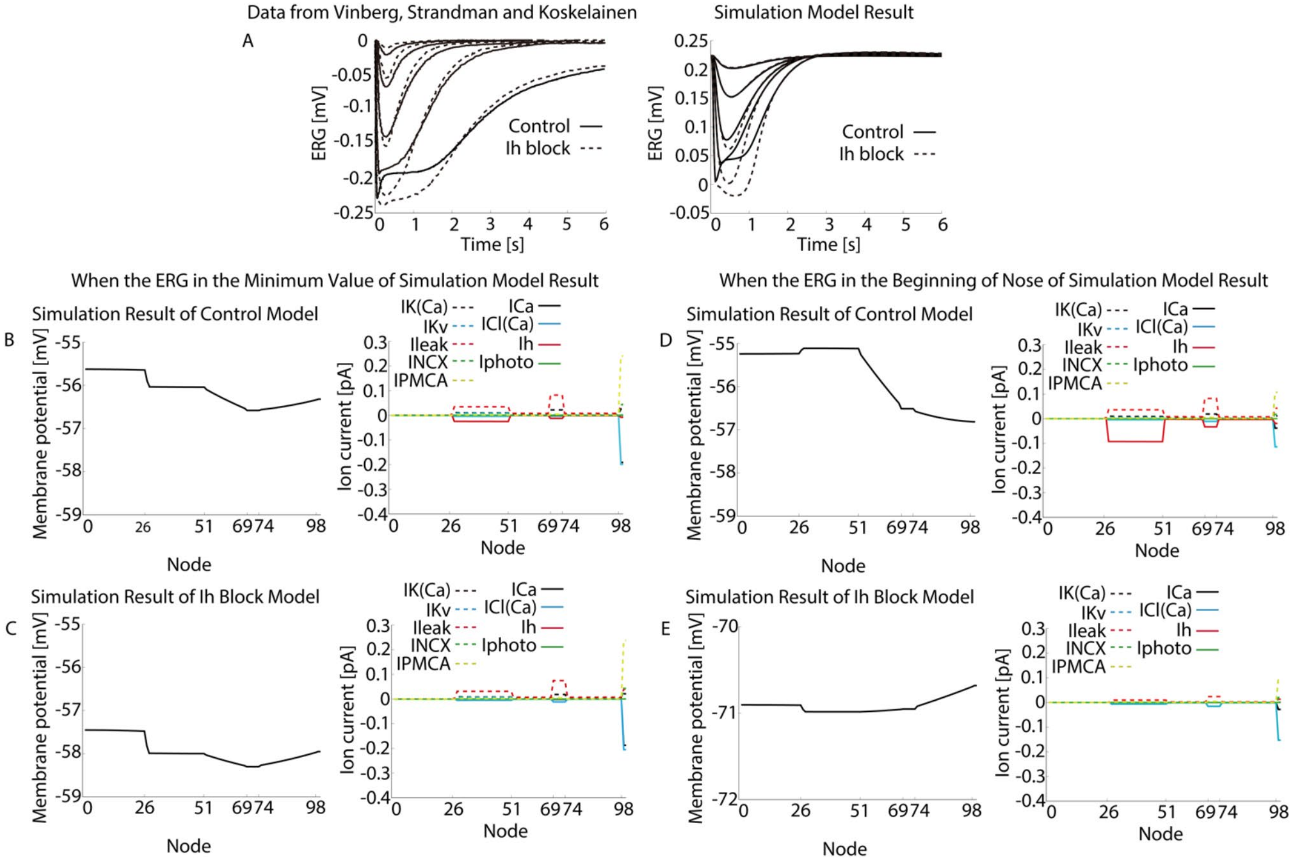

Fig. 8. (**A**) Comparison of electroretinogram (ERG) responses with and without I_h blockage. Data derived from experiments conducted by Vinberg, Strandman, and Koskelainen are presented on the upper panel, with model results shown on the lower panel[28]. Solid lines represent control conditions, whereas dashed lines indicate the responses with I_h blockage. (**B**–**E**) Detailed membrane potential, and profiles of the individual ion current components such as $I_{K(Ca)}$, I_{Ca}, I_{Kv}, $I_{Cl(Ca)}$, I_{leak}, I_h, I_{NCX}, I_{photo}, and I_{PMCA}, at specified time. Simulation results of control model (**B**) and I_h block model (**C**) when the ERG is at minimum value; simulation results of control model (**D**) and I_h block model (**E**) when the ERG is in the beginning of the "nose."

At the beginning of the ERG recovery process, when the "nose" appeared (t_3 in Fig. 7A), no current was observed in the OS (Fig. 7D). The ion channel currents in other areas gradually decreased. The most apparent change was the significant reduction in the I_{PMCA}, I_{Ca}, and $I_{Cl(Ca)}$ of the ST; interestingly, there was a significant increase in the I_h of the IS and CB.

During the ERG recovery process at the end of the "nose" (t_4 in Fig. 7A), the change trends of most ion channel currents were almost similar to those at the beginning of the "nose" (Fig. 7E). The only difference was that I_{photo} of the OS began to increase.

By the end of the recovery phase, when the waveform almost returned to the dark state (t_5 in Fig. 7A), the currents of each ion channel in each compartment were similar to their dark-state amplitudes (Fig. 7F).

I_h channel block

Vinberg et al. reported transretinal ERG waveforms of rod photoreceptor cells in mice with and without an I_h channel block (Fig. 8A, left panel)[28]. This was achieved by the administration of APB or aspartate to block bipolar cell activity, and ZD7288 to block the I_h channel. We reproduced the photoreceptor component of the transretinal ERG waveform with an I_h channel block by applying light stimulation of 4, 15, 50, 130, and 1,000 Rh*/s under dark adaptation. The resulting ERG waveforms are shown in the right panel of Fig. 8A. The simulation results showed waveforms similar to those reported by Vinberg et al. This result supports the idea suggested by Vinberg et al., that the main origin of the "nose" component is related to the I_h channel current.

To understand the mechanism of "nose" generation on the ERG waveform, we used a high-light intensity condition (1,000 Rh*/s) and compared the simulation results between the control and I_h block models. For these two conditions, the distribution of the membrane potential and the individual ion currents in each compartment of the membrane current at two specific time points, when the ERG is at the minimum value and when the ERG is in the beginning of the "nose," are shown in Fig. 8B–E, respectively.

When the ERG was at its minimum value, the membrane potential difference between the control model and I_h block model was only 2 mV and the potential distributions were similar (left of Fig. 8B,C). The distribution and amplitude of the individual ion currents in each compartment showed no significant differences between the two models (Fig. 8B,C).

During the ERG recovery phase at the beginning of the "nose," the membrane potential difference between the control model and I_h block model became 15 mV, and its distributions were completely different (left of Fig. 8D,E). It can be observed that in the control model, the membrane potential distribution increased slightly from the OS to the IS and then consistently decreased until it reached the ST, but the difference was ~ 2 mV. However, in the I_h block model, the membrane potential reached ~ 71 mV, and its distribution decreased slightly from the OS to the IS, and then consistently increased until it reached the ST. There was almost no difference between the lowest membrane potential in the IS and the highest in the ST. Furthermore, the distribution of the individual ion currents in each compartment at this time showed some differences, such as all the I_h currents became zero, the I_{leak} currents in the IS and CB became smaller, and the $I_{Cl(Ca)}$ currents in the ST became larger (right of Fig. 8B,C). A detailed analysis of these differences is presented in the Discussion section, where we used extracellular current loop diagrams to explore the relationships between ion channel currents in different compartments and the possible causes of these differences (Fig. 9).

Discussion

It is well-known that Ca^{2+} flux via I_{photo} is extruded by NCKX[44]. In the I_{photo} of the proposed model, Ca^{2+} homeostasis may not be achievable. To further evaluate the effects of extracellular and intracellular ion concentrations, they must be adjusted to a model that balances these effects against those of other ions. Nevertheless, our analyses found that the I_{photo} current model reproduced the ERG waveform well (Figs. 5 and 8), which is considered to be the major component of the photoreceptor contribution to the ERG waveform. Therefore, the I_{photo} current model remains useful as the base model for ERG generation because the proposed model is intended as a basic platform for examining the relationships between photoreceptor cell ion currents and the ERG waveform. However, the components of this photoreceptor cell model require further investigation.

Conventionally, the photoreceptor component of an ERG is believed to be dominated by the I_{photo} current[64]. Our comparison of the waveforms of I_{photo} and the ERG found that the two were highly similar when the intensity of the light stimulus was low (Fig. 5). In contrast, when the light intensity was higher, a "nose" shape was observed, with a steep positive component generated immediately after the steep negative component that directly followed light stimulation. It was confirmed that the "nose" differed from the shape of the I_{photo} waveform at these time points (Fig. 5). From this, we can infer that other elements work with I_{photo} to dominate

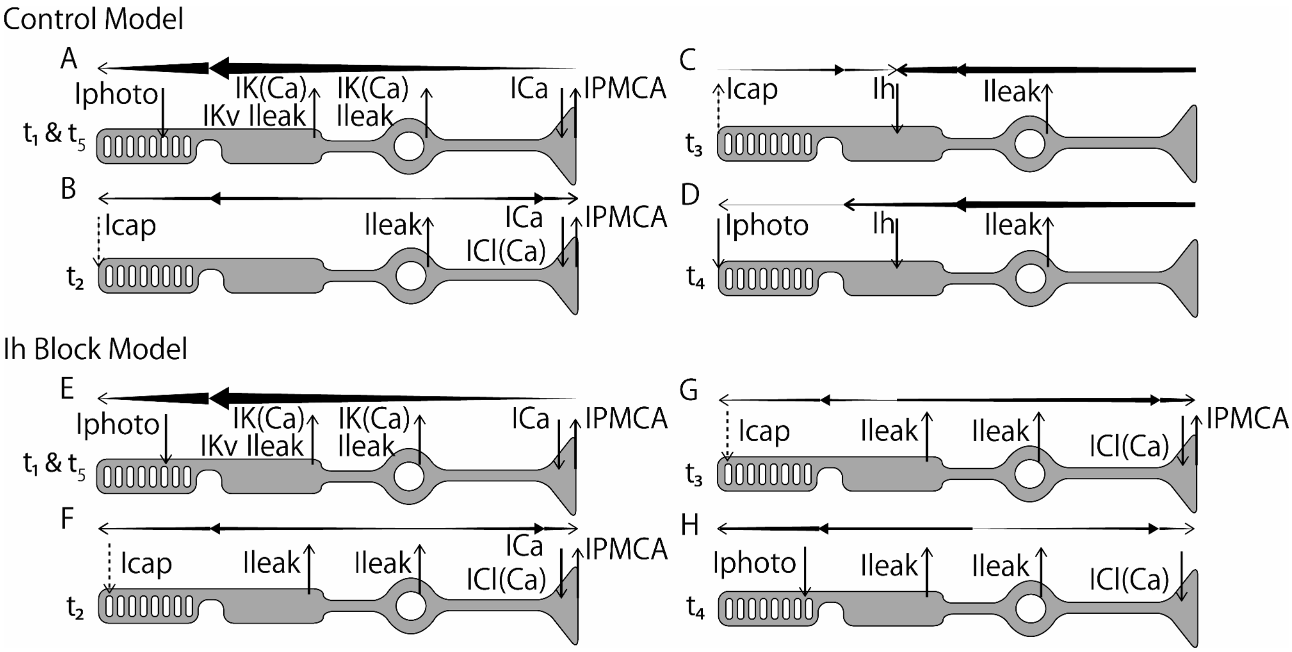

Fig. 9. Relationships between the specific ion channel current and extracellular current in a rod photoreceptor cell model. The figures represent the specific ion channel current for each compartment and the flow of the extracellular current at different times when the proposed and the I_h-blocked models are subjected to light simulation intensity of 10,000 Rh*/s for 20 ms (Fig. 6A). The arrow above the photoreceptor cell represents the extracellular current and its thickness represents the magnitude of the current. From left to right, the compartments shown are the OS, OSIS, IS, ISCB, CB, AX, and ST, and the current flow direction of the channel mounted at specific compartment is represented by an arrow, with the thickness representing the magnitude of the current. (**A**–**D**) The control model; (**E**–**H**) the I_h-blocked model. (**A**, **E**) The dark state, and the recovered condition after light simulation; (**B**, **F**) the state with the lowest electroretinogram (ERG) due to light stimulation; (**C**, **G**) the state at the start of the "nose;" (**D**, **H**) the state at the end of the "nose."

the photoreceptor component of the ERG waveform. These "hidden" dominant elements do not affect the shape of the ERG waveform more than I_{photo} when the light stimulus is of low intensity.

Although there have been many studies on ion channels in each component of rod photoreceptor cells, very few have studied the distribution of ion channels across the whole cell and the currents after light stimulation, represented by the formation of the ERG waveform. Changes in currents corresponding to temporal variations are yet to be elucidated. Based on the results shown in Figs. 6 and 7, we analyzed the ion currents in different cell compartments and the extracellular currents of the whole cell (Fig. 9).

In the dark, the extracellular current flows out of the ST toward the OS. The extracellular current reaches its peak value upon reaching the IS. It enters the rod photoreceptor cell through I_{photo} in the OS, forming a current loop (Fig. 9A).

Following light stimulus, the ERG gradually decreases. When it reaches its lowest value, the extracellular current flows out of the CB and reenters the cell through the capacitive currents (I_{cap}, dashed line) in the OS, and the ion currents in the ST form two smaller current loops (Fig. 9B).

During the subsequent recovery of the ERG, the extracellular current loop gradually begins two current loops, and the extracellular current flows out through I_{cap} in the OS and then reenters the cell mainly through I_h in the IS (Fig. 9C). The "nose" is generated when an extracellular current is present in these two current loops.

The extracellular current loop then becomes one current loop but still reenters the cell mainly through I_h in the IS (Fig. 9D).

Finally, the extracellular current loop returns to the pattern formed by the outflow from the ST and inflow through the I_{photo} of the OS (Fig. 9A).

Our analysis agrees with the theoretically predicted currents described by Robson, adding credence to this experiment and our model[32]. However, although the extracellular current loops can be reproduced by our proposed model to some extent (because the actual ion channel distribution of each compartment is hypothetical), whether the relevant ion channels leading to the changes in these current loops are related to I_{PMCA}, I_{Ca}, or I_h needs to be confirmed by future studies on the existence of ion channels in each rod photoreceptor cell compartment.

To analyze the reasons behind the membrane potential differences observed between the I_h-blocked and control models simultaneously, we also investigated the ion currents in different cell compartments and the extracellular currents of the whole cell in the I_h-blocked model.

As shown in Fig. 9E,F, the extracellular current loops in the I_h-blocked model resembled those in the control model before the "nose" waveform appeared after light stimulation. This suggests that I_h does not play a significant role when the membrane potential is high.

However, at t_3, when the "nose" waveform was expected to occur, the extracellular current loops remained consistent, as at t_2, they flowed outward from the IS and inward through the OS and ST, respectively (Fig. 9G). Even at t_4, when the "nose" waveform ended, these current loops persisted (Fig. 9H). This indicates that in the absence of I_h, a pathway for the extracellular current to re-enter the cell is missing, resulting in a continuous outflow of intracellular current to the extracellular space. This ultimately leads to a progressive decrease in the membrane potential. These findings highlight the critical role of I_h in maintaining membrane potential stability.

Combined with the analysis of the model characteristics in Figs. 6 and 7, and 9 (especially the changes between t_2 and t_3), it can be seen that, when subjected to high-intensity light stimulation, the rapid rise in ERG after reaching the valley was mainly caused by the effect of I_h. This was an analysis of the positive components of the "nose." Through the same analysis, it was hoped that the steep negative components generated by the stimulation with high light intensity would be completely dominated by I_{photo}. If not, there should be other "hidden" dominant elements that affect the change of the ERG.

After stimulation by high-intensity light, as shown in Fig. 10A, the time required for the ERG to reach the valley value (t_2) from the dark state (t_1) was 45 ms (black arrow). To confirm the characteristics of the model between t_1 and t_2, we defined points t_{n1}–t_{n10} at intervals of 5 ms between t_1 and t_2. The red line represents the "baseline value" which is the plateau ERG after receiving high-intensity light stimulation, and below the red line is the "nose." According to Fig. 10B, the ERG also continued to decline after t_{n6} owing to the continuous shrinking of the extracellular potential difference between the OS and ST. According to Fig. 10C, although the extracellular current decreased, the extracellular current circuit did not change significantly at this time.

By analyzing the ion current composition (Fig. 10D,F), it can be found that when it is about to reach the red line, that is, after being stimulated by light for 25 ms (t_{n6}), the I_{photo} in the OS almost decreases to zero. Immediately after 5 ms (t_{n7}), I_{photo} in the OS was zero. In other words, I_{photo} did not dominate "nose" formation.

Figure 10E shows that after I_{photo} becomes zero, the extracellular current is stored in the OS in the form of a capacitive current; therefore, the extracellular current can still enter the cell at the OS, and the extracellular potential difference between the OS and ST continues to decrease. Thus, the factor that has an important impact on the change of ERG other than I_{photo} is the capacitive current in the OS (that is, the "hidden" dominant element). This factor allows the extracellular current circuit to be maintained for a short period after I_{photo} does not function, causing the ERG to leave a "baseline value" and continue declining, forming the main negative component of the "nose." After that, the influence of I_h current gradually increases, and coupled with the influence of the capacitive current between the IS and ST, returns the ERG to the "baseline value," forming the main positive component of the "nose."

Using the proposed model, the ion and capacitive currents of various compartments of the rod photoreceptor cell were quantitatively analyzed. The results not only have no obvious contradiction with the existing research reports but also further improve the understanding of the relationship between the current composition in the rod photoreceptor cell and ERG[19,32].

To improve the fit of the ERG of the simulation model result from the OS to the IS in Fig. 5C to the reported experimental data, given that only I_{photo} was present in the OS and only I_{leak} was present in the OSIS, adjustments

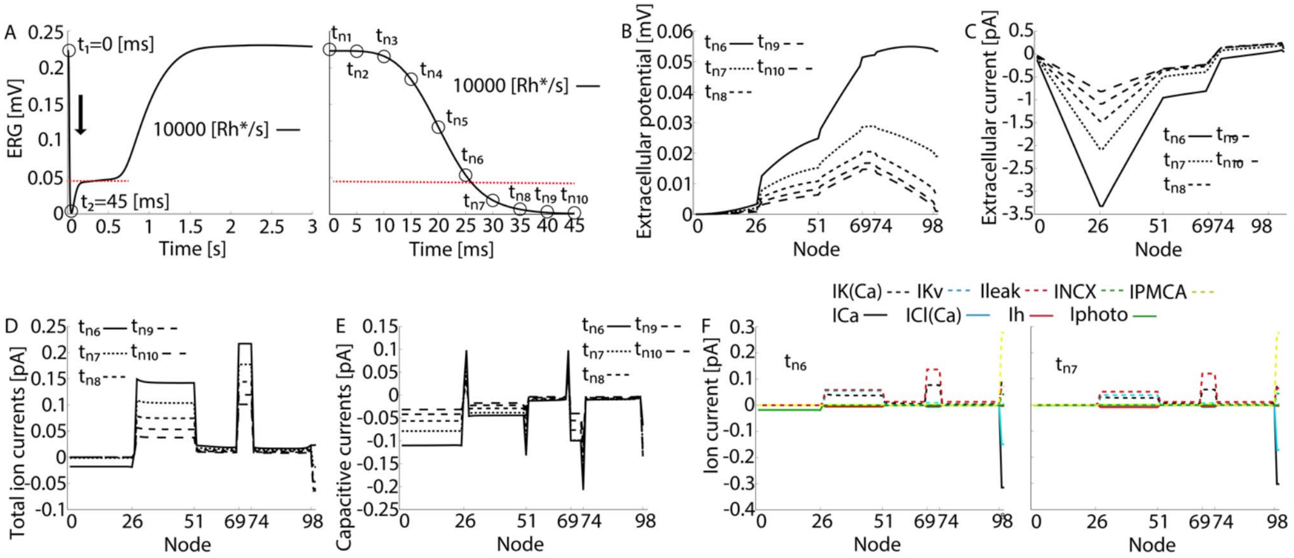

Fig. 10. Analysis of the waveform characteristics when the electroretinogram (ERG) drops to the valley value after being stimulated by high-intensity light. (**A**) when the light stimulation intensity is 10,000 Rh*/s, the overall ERG changes (left) from the dark state decline to the valley value (right). (**B**–**E**) Extracellular potential, extracellular current, total ion currents, and capacitive currents, respectively, at different time points (t_{n6} though t_{n10}) across the rod photoreceptor's node. (**F**) Detailed profiles of the individual ionic current components such as $I_{K(Ca)}$, I_{Ca}, I_{Kv}, $I_{Cl(Ca)}$, I_{leak}, I_{h}, I_{NCX}, I_{photo}, and I_{PMCA}, at specified time points (t_{n6} and t_{n7}).

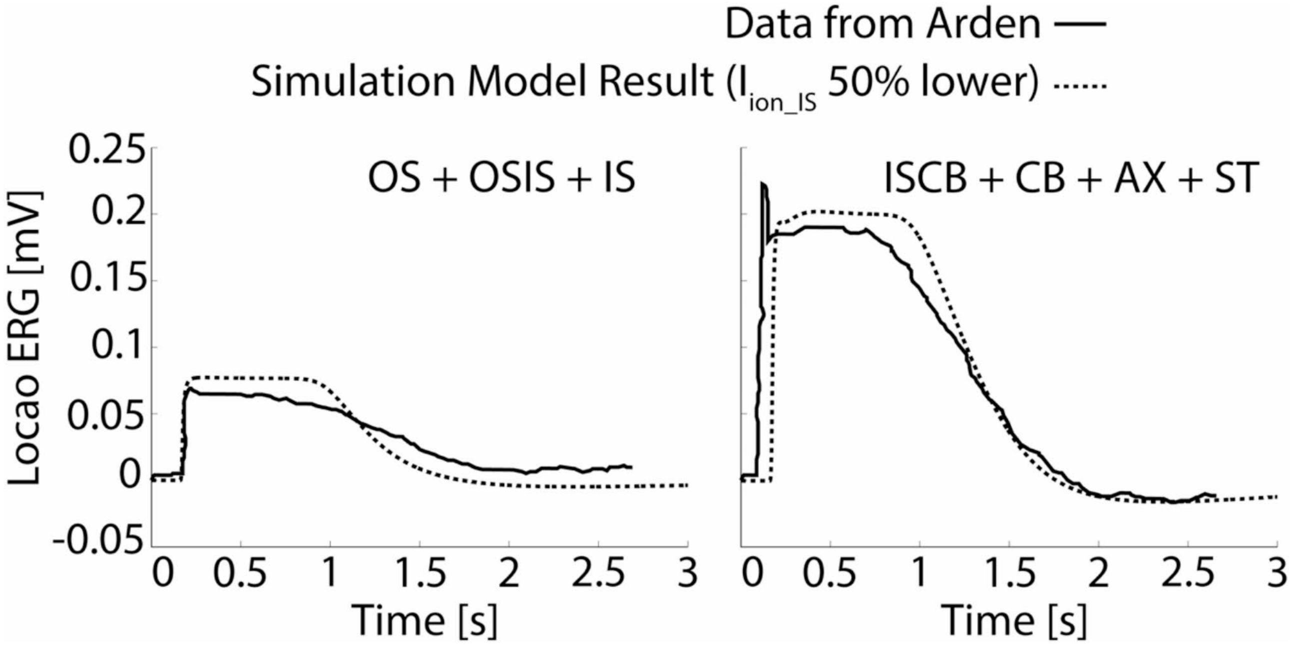

Fig. 11. Local electroretinogram (ERG) data from Arden[63], comparing all compartments to specific regions within the rod photoreceptor cells, with solid lines representing experimental data and dotted lines indicating model results. The results of suppressing all outward currents of the IS at 50% and increasing the suppressed amount to other distributed forms are re-compared with experimental data.

were made to reduce each outward ion current in the IS by 50% proportionally, aiming to decrease the ERG. Additionally, the outward ion currents correspondingly increased in other distributed regions. This implies that the discrepancy in the ERG of the simulation model resulting from the ISCB to the ST in Fig. 5C, which is lower than the experimental data, might also be improved. According to the adjusted results (Fig. 11, dotted lines), the ERG from the OS to the IS reduced, aligning more closely with the reported experimental data. Although the ERG from the ISCB to the ST increased significantly, the "nose" waveform disappeared. From these results, it

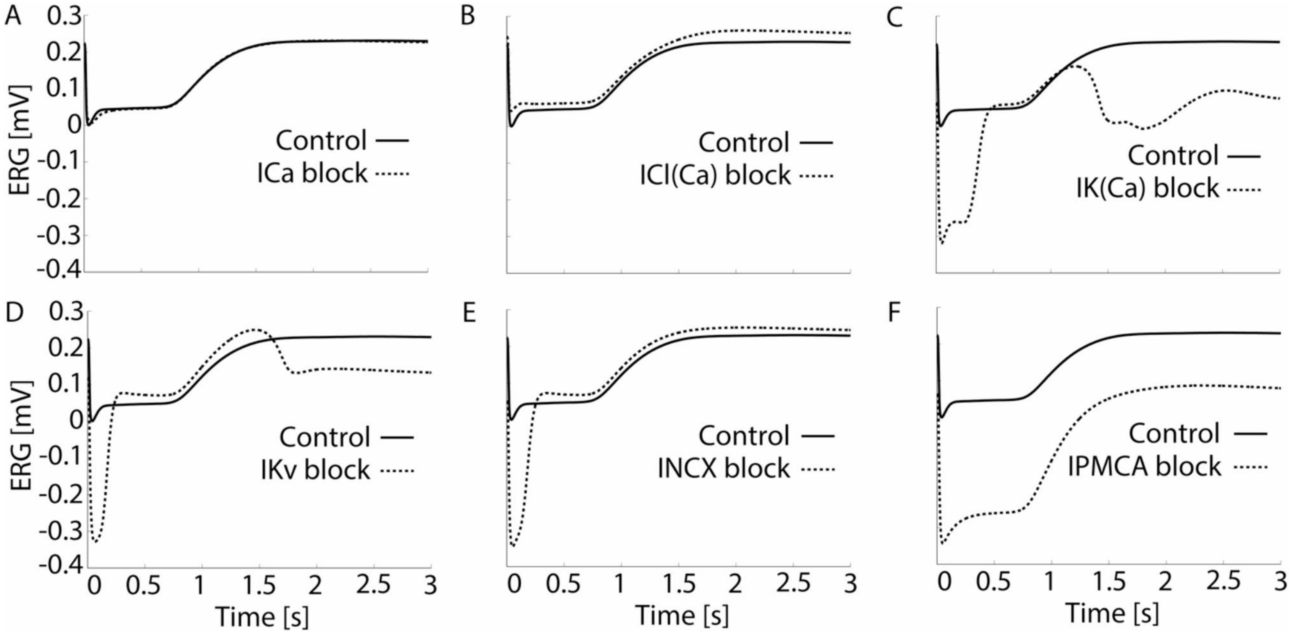

Fig. 12. Impact of ion channel current blocks on the electroretinogram (ERG) waveform. Each graph displays the ERG response over a time span of 3 s under control conditions (solid line) compared to conditions of specific ionic current inhibition (dotted line). (**A**) I_{Ca} block; (**B**) $I_{\mathrm{Cl(Ca)}}$ block; (**C**) $I_{\mathrm{K(Ca)}}$ block; (**D**) I_{Kv} block; (**E**) I_{NCX} block; (**F**) I_{PMCA} block.

is evident that adjusting the magnitude of the ERG using the model can be relatively straightforward. However, adjusting specific waveform shapes appears to be more challenging. Future advancements in research on ion channel distributions or ion current magnitudes may allow our proposed model to be adjusted. Despite the model being at a hypothetical stage in this study, the experimental results demonstrate high operability and reproducibility.

One of the experimental results of this study was the successful reproduction of the effects of inhibiting the I_{h} channel on the changes in the ERG waveform. Additionally, we analyzed the impact of inhibiting the I_{h} channel during the recovery process of the waveform after the ERG reached its minimum until it began to rise again, as induced by light stimulation. According to the results shown in Fig. 8, the I_{h} channel plays a crucial role in controlling the membrane potential, thereby affecting the activation of other ion channel currents and resulting in the generation of the "nose" on the ERG. Notably, Fig. 8A shows that in the I_{h} block condition, the "nose" after the minimum value was delayed compared to the control, indicating a slower recovery process. While Fig. 8B,C reveal similar membrane potentials at the minimum value, the difference in Fig. 8D,E highlights the continued activity of $I_{\mathrm{Cl(Ca)}}$ in the I_{h} block model, leading to a further membrane potential decline and a negative ERG value. Additionally, the right panel of Fig. 8A shows a faster response than our model results shown in the left panel, suggesting possible discrepancies in ion channel distribution or time constants in the model compared with physiological conditions[28].

However, besides I_{h}, significant changes were observed in the outward current I_{PMCA} and inward currents I_{Ca} and $I_{\mathrm{Cl(Ca)}}$ in the ST. Because of this notable change, we consider that these three ion channel currents also influence "nose" generation. Therefore, we conducted individual inhibition experiments for each ion channel to analyze whether factors other than I_{h} are related to "nose" generation. During these experiments, I_{photo} and I_{leak} were not included; the former only exists in the OS, and inhibiting it leads to no response, whereas the latter, strictly speaking, is not an identified ion channel, and its mechanism remains unclear. Hence, we only inhibited I_{Ca}, $I_{\mathrm{Cl(Ca)}}$, $I_{\mathrm{K(Ca)}}$, I_{Kv}, I_{NCX}, or I_{PMCA}.

As shown in Fig. 12, the differential modulation of the ERG waveform reveals the complex interaction of various ion channel currents in shaping the electrical response of rod photoreceptor cells. In the case of blocking I_{Ca}, the change in ERG amplitude showed that I_{Ca} had little impact on the formation of rod-photoreceptor cell components in the ERG waveform (Fig. 12A). The same result was observed when $I_{\mathrm{Cl(Ca)}}$ was blocked; however, the overall ERG amplitude was slightly lower (Fig. 12B). In contrast, changes in the waveform after blocking $I_{\mathrm{K(Ca)}}$, I_{Kv}, I_{NCX}, and I_{PMCA} highlighted the formation of these ion channel currents as rod photoreceptor cell components in the ERG waveform and their contribution to the photostimulation response process (Fig. 12C–F). If any of these four ion channels are blocked when the rod photoreceptor cells are stimulated by light, the ERG will become negative, which means that there will still be a potential difference between the OS and ST and not just the disappearance of the potential difference between the OS and ST, resulting in an ERG amplitude close to zero. At this time, the extracellular potential at the OS is high, and ST is low, and the extracellular current circuit is formed from the OS to ST. The difference between these four situations is that the ERG waveform is in an unstable state when after blocking $I_{\mathrm{K(Ca)}}$ or I_{Kv}, the rod photoreceptor cells are stimulated by light and return to the dark state. The final recovery of the ERG amplitude was lower than that obtained without blocking $I_{K(Ca)}$ or I_{Kv}. In contrast, after blocking I_{NCX}, the rod photoreceptor cells are stimulated by light, although there will be a negative ERG amplitude. In the process of returning to the dark state, it almost coincides with the ERG waveform obtained by non-blocking I_{NCX}. After blocking I_{PMCA}, rod photoreceptor cells are stimulated by light and return to a dark state. During this process, the overall ERG waveform is almost the same; however, the amplitude is much lower and negative.

Although the results in Fig. 12 do not conclusively demonstrate the relationship between other ion currents and the origin of the "nose," the inhibition of individual ion currents is reflected in the changes observed in the ERG waveform, especially in the I_{Kv} block condition[18]. However, in the proposed model, only the minimum calcium ion transport mechanism was used to maintain intracellular calcium homeostasis. It is necessary to make appropriate modifications or updates to the mechanism of calcium ion transport. Simultaneously, other necessary ion transport mechanisms, such as sodium, potassium, and chloride ions, must be installed in the model. In general, these findings emphasize the need for a multifaceted perspective on ion contribution when building a mathematical model of rod photoreceptor cells to accurately replicate retinal electrophysiological phenomena.

In the proposed model, the rod photoreceptor structure comprises seven compartments. The ion channel model was distributed across each compartment, according to previously reported information on ion channel distribution. However, depending on the experimental approach and species, various ion channel distribution results can be obtained. Therefore, the ion channel distribution in the proposed model is largely hypothetical and is likely to be somewhat different from the actual distribution. However, it should also be noted that the proposed model is based on the Kamiyama model, which can reproduce real ERG results. We also considered the results of subsequent studies on the distribution of ion channels and successfully reproduced previously reported ERG waveforms and related experimental results. Therefore, the ion channel distribution in the model did not appear to have a significant influence on the essential results. In the future, with increased data on the ion channel distribution of rod photoreceptor cells, the ion channel distribution of our model can be updated or modified to reflect this additional information, and changes in the newly obtained ERG waveforms can be analyzed. Additionally, further refinement of the Ca^{2+} diffusion model will be incorporated to better capture intracellular calcium dynamics.

Data availability

All data generated or analyzed during this study are included in this published article. The datasets used and/or analyzed during the current study available from the corresponding author on reasonable request.

Received: 17 October 2024; Accepted: 25 March 2025

References

1. Grossniklaus, H. E., Geisert, E. E. & Nickerson, J. M. Introduction to the retina. *Prog Mol. Biol. Transl Sci.* **134**, 383–396 (2015).
2. Riggs, L. A. & Electroretinography *Vis. Res.* **26**(9), 1443–1459 (1986).
3. Karpe, G. The basis of clinical electroretinography. *Acta Ophthalmol.* **24**, 1–118 (1945).
4. Mahroo, O. A. Visual electrophysiology and the potential of the potentials. *Eye (Lond).* **37** (12), 2399–2408 (2023).
5. Tomita, T. & Yanagida, T. Origins of the ERG waves. *Vis. Res.* **21** (11), 1703–1707 (1981).
6. Granit, R. The components of the retinal action potential in mammals and their relation to the discharge in the optic nerve. *J. Physiol.* **77** (3), 207–239 (1933).
7. Pepperberg, D. R. & Masland, R. H. Retinal-induced sensitization of light-adapted rabbit photoreceptors. *Brain Res.* **151** (1), 194–200 (1978).
8. Hood, D. C. & Birch, D. G. A quantitative measure of the electrical activity of human rod photoreceptors using electroretinography. *Vis. Neurosci.* **5** (4), 379–387 (1990).
9. Hood, D. C. & Birch, D. G. The a-wave of the human electroretinogram and rod receptor function. *Invest. Ophthalmol. Vis. Sci.* **31** (10), 2070–2081 (1990).
10. Hood, D. C. & Birch, D. G. A computational model of the amplitude and implicit time of the b-wave of the human ERG. *Vis. Neurosci.* **8** (2), 107–126 (1992).
11. Hood, D. C. & Birch, D. G. Light adaptation of human rod receptors: The leading edge of the human a-wave and models of rod receptor activity. *Vis. Res.* **33** (12), 1605–1618 (1993).
12. Vinberg, F., Kolesnikov, A. V. & Kefalov, V. J. Ex vivo ERG analysis of photoreceptors using an in vivo ERG system. *Vis. Res.* **101**, 108–117 (2014).
13. Fujii, M., Sunagawa, G. A., Kondo, M., Takahashi, M. & Mandai, M. Evaluation of micro electroretinograms recorded with multiple electrode array to assess focal retinal function. *Sci. Rep.* **6**, 30719 (2016).
14. Pahlberg, J. et al. Voltage-sensitive conductances increase the sensitivity of rod photoresponses following pigment bleaching. *J. Physiol.* **595** (11), 3459–3469 (2017).
15. Creel, D. J. Electroretinograms *Handb. Clin. Neurol.* **160**, 481–493 (2019).
16. Inamdar, S. M. et al. Differential impact of Kv8.2 loss on rod and cone signaling and degeneration. *Hum. Mol. Genet.* **31** (7), 1035–1050 (2022).
17. Perlman, I. in *The Electroretinogram: ERG. Webvision: The Organization of the Retina and Visual System*. (eds Kolb, H., Fernandez, E. & Nelson, R.) (University of Utah Health Sciences Center, 2001).
18. Kang Derwent, J. J. & Linsenmeier, R. A. Intraretinal analysis of the a-wave of the electroretinogram (ERG) in dark-adapted intact Cat retina. *Vis. Neurosci.* **18** (3), 353–363 (2001).
19. Bhatt, Y., Hunt, D. M. & Carvalho, L. S. The origins of the full-field flash electroretinogram b-wave. *Front. Mol. Neurosci.* **16**, 1153934 (2023).
20. Shahi, P. K. et al. Abnormal electroretinogram after Kir7.1 channel suppression suggests role in retinal electrophysiology. *Sci. Rep.* **7** (1), 10651 (2017).
21. Haq, W., Zrenner, E., Ueffing, M. & Paquet-Durand, F. Using Micro-electrode-array recordings and retinal disease models to elucidate visual functions: Simultaneous recording of local electroretinograms and ganglion cell action potentials reveals the origin of retinal oscillatory potentials. *Bioeng. (Basel).* **10** (6), 725 (2023).

22. Asi, H. & Perlman, I. Relationships between the electroretinogram a-wave, b-wave and oscillatory potentials and their application to clinical diagnosis. *Doc. Ophthalmol.* **79** (2), 125–139 (1992).
23. Jiang, X. & Mahroo, O. A. Negative electroretinograms: Genetic and acquired causes, diagnostic approaches and physiological insights. *Eye (Lond).* **35** (9), 2419–2437 (2021).
24. Honda, T. et al. Proportions of diseases with definite diagnoses by ERG in patients with vision loss for unknown reason. *Japn. Orthoptic J.* **42**, 109–113 (2013).
25. Miyake, Y., Yagasaki, K., Horiguchi, M., Kawase, Y. & Kanda, T. Congenital stationary night blindness with negative electroretinogram. A new classification. *Arch. Ophthalmol.* **104** (7), 1013–1020 (1986).
26. Pardue, M. T., McCall, M. A., LaVail, M. M., Gregg, R. G. & Peachey, N. S. A naturally occurring mouse model of X-linked congenital stationary night blindness. *Invest. Ophthalmol. Vis. Sci.* **39** (12), 2443–2449 (1998).
27. Jamison, J. A., Bush, R. A., Lei, B. & Sieving, P. A. Characterization of the rod photoresponse isolated from the dark-adapted primate ERG. *Vis. Neurosci.* **18** (3), 445–455 (2001).
28. Vinberg, F. J., Strandman, S. & Koskelainen, A. Origin of the fast negative ERG component from isolated aspartate-treated mouse retina. *J. Vis.* **9** (12), 1–17 (2009).
29. Zhao, D. et al. Retinal dysfunction in a mouse model of HCN1 genetic epilepsy. *J. Neurosci.* **43** (12), 2199–2209 (2023).
30. Brzezinski, J. A. & Reh, T. A. Photoreceptor cell fate specification in vertebrates. *Development* **142** (19), 3263–3273 (2015).
31. Jiang, X. et al. Molecular, cellular and functional changes in the retinas of young adult mice lacking the voltage-gated K+ channel subunits Kv8.2 and K2.1. *Int. J. Mol. Sci.* **22** (9), 4877 (2021).
32. Robson, J. G. & Frishman, L. J. The rod-driven a-wave of the dark-adapted mammalian electroretinogram. *Prog. Retin. Eye Res.* **39**, 1–22 (2014).
33. Tyler, C. W. Advanced computational model of rod ERG kinetics. *Doc. Ophthalmol.* **149** (1), 1–10 (2024).
34. Kamiyama, Y., Ogura, T. & Usui, S. Ionic current model of the vertebrate rod photoreceptor. *Vis. Res.* **36** (24), 4059–4068 (1996).
35. Kamiyama, Y., Wu, S. M. & Usui, S. Simulation analysis of bandpass filtering properties of a rod photoreceptor network. *Vis. Res.* **49** (9), 970–978 (2009).
36. Morgans, C. W., El, F. O., Berntson, A., Wässle, H. & Taylor, W. R. Calcium extrusion from mammalian photoreceptor terminals. *J. Neurosci.* **18** (7), 2467–2474 (1998).
37. Steele, E. C. Jr., Chen, X. & MacLeish, P. R. Fluoxetine inhibits calcium-activated currents of salamander rod photoreceptor Somata and presynaptic terminals via modulation of intracellular calcium dynamics. *Mol. Vis.* **11**, 1200–1210 (2005).
38. Kizhatil, K., Sandhu, N. K., Peachey, N. S. & Bennett, V. Ankyrin-B is required for coordinated expression of beta-2-spectrin, the Na/K-ATPase and the Na/Ca exchanger in the inner segment of rod photoreceptors. *Exp. Eye Res.* **88** (1), 57–64 (2009).
39. Stöhr, H. et al. TMEM16B, a novel protein with calcium-dependent chloride channel activity, associates with a presynaptic protein complex in photoreceptor terminals. *J. Neurosci.* **29** (21), 6809–6818 (2009).
40. Tanimoto, N. et al. BK channels mediate pathway-specific modulation of visual signals in the in vivo mouse retina. *J. Neurosci.* **32** (14), 4861–4866 (2012).
41. Knoflach, D. et al. Cav1.4 IT mouse as model for vision impairment in human congenital stationary night blindness type 2. *Channels (Austin)* **7** (6), 503–513 (2013).
42. Jeon, J. H., Paik, S. S., Chun, M. H., Oh, U. & Kim, I. B. Presynaptic localization and possible function of calcium-activated chloride channel anoctamin 1 in the mammalian retina. *PLoS One* **8** (6), e67989 (2013).
43. Caputo, A. et al. TMEM16A is associated with voltage-gated calcium channels in mouse retina and its function is disrupted upon mutation of the auxiliary A2δ4 subunit. *Front. Cell. Neurosci.* **9**, 422 (2015).
44. Fortenbach, C. et al. Loss of the K + channel Kv2.1 greatly reduces outward dark current and causes ionic dysregulation and degeneration in rod photoreceptors. *J. Gen. Physiol.* **153** (2), e202012687 (2021).
45. Torre, V., Forti, S., Menini, A. & Campani, M. Model of phototransduction in retinal rods. *Cold Spring Harb Symp. Quant. Biol.* **55**, 563–573 (1990).
46. Abtout, A., Fain, G. & Reingruber, J. Analysis of waveform and amplitude of mouse rod and cone flash responses. *J. Physiol.* **599** (13), 3295–3312 (2021).
47. Yamada, W. M., Koch, C. & Adams, P. R. Multiple channels and calcium dynamics. in *Methods in Neuronal Modeling: From Ions to Networks* (eds. Koch, C. & Segev, I.) 97–133 (MIT Press, 1989).
48. DiFrancesco, D. & Noble, D. A model of cardiac electrical activity incorporating ionic pumps and concentration changes. *Philos. Trans. R Soc. Lond. B Biol. Sci.* **307** (1133), 353–398 (1985).
49. Rodieck, R. W. *The First Steps in Seeing* (Sinauer Associates, 1998).
50. Zampighi, G. A. et al. Conical tomography of a ribbon synapse: structural evidence for vesicle fusion. *PLoS One* **6** (3), e16944 (2011).
51. Hoang, Q. V., Linsenmeier, R. A., Chung, C. K. & Curcio, C. A. Photoreceptor inner segments in monkey and human retina: Mitochondrial density, optics, and regional variation. *Vis. Neurosci.* **19** (4), 395–407 (2002).
52. Hsu, A., Tsukamoto, Y., Smith, R. G. & Sterling, P. Functional architecture of primate cone and rod axons. *Vis. Res.* **38** (17), 2539–2549 (1998).
53. Chang, E. T. Y. Towards Understanding the electrogram: Theoretical and experimental multiscale modelling of factors affecting action potential propagation in cardiac tissue. *Imperial Coll. Lond.* https://doi.org/10.25560/12792 (2013).
54. Hagins, W. A., Penn, R. D. & Yoshikami, S. Dark current and photocurrent in retinal rods. *Biophys. J.* **10** (5), 380–412 (1970).
55. Johnson, J. E. Jr. et al. Spatiotemporal regulation of ATP and Ca2 + dynamics in vertebrate rod and cone ribbon synapses. *Mol. Vis.* **15**, 13, 887–919 (2007).
56. Clark, B. S. et al. Single-cell RNA-Seq analysis of retinal development identifies NFI factors as regulating mitotic exit and Late-Born cell specification. *Neuron* **102** (6), 1111–1126 (2019).
57. Van, Hook, M. J., Nawy, S. & Thoreson, W. B. Voltage- and calcium-gated ion channels of neurons in the vertebrate retina. *Prog. Retin. Eye Res.* **72**, 100760 (2019).
58. Beeler, G. W. & Reuter, H. Reconstruction of the action potential of ventricular myocardial fibres. *J. Physiol.* **268** (1), 177–210 (1977).
59. Skouibine, K. B., Trayanova, N. A. & Moore, P. K. Anode/cathode make and break phenomena in a model of defibrillation. *IEEE Trans. Biomed. Eng.* **46** (7), 769–777 (1999).
60. Vigmond, E. J., Hughes, M., Plank, G. & Leon, L. J. Computational tools for modeling electrical activity in cardiac tissue. *J. Electrocardiol.* **36**, 69–74 (2003).
61. Plank, G. et al. Algebraic multigrid preconditioner for the cardiac bi-domain model. *IEEE Trans. Biomed. Eng.* **54** (4), 585–596 (2007).
62. Southern, J. A., Plank, G., Vigmond, E. J. & Whiteley, J. P. Solving the coupled system improves computational efficiency of the bi-domain equations. *IEEE Trans. Biomed. Eng.* **56** (10), 2404–2412 (2009).
63. Arden, G. B. Voltage gradients across the receptor layer of the isolated rat retina. *J. Physiol.* **256** (2), 333–360 (1976).
64. Hüttl, S. et al. Impaired channel targeting and retinal degeneration in mice lacking the cyclic nucleotide-gated channel subunit CNGB1. *J. Neurosci.* **25** (1), 130–138 (2005).

Author contributions

S.O. and K.H. developed and analyzed the model and drafted the manuscript. Y.M., Y.H. and S.T. validated the model and revised the manuscript. A.A. supervised the study and revised the manuscript. All authors reviewed and approved the manuscript.

Declarations

Competing interests

The authors declare no competing interests.

Additional information

Correspondence and requests for materials should be addressed to A.A.

Reprints and permissions information is available at www.nature.com/reprints.

Publisher's note Springer Nature remains neutral with regard to jurisdictional claims in published maps and institutional affiliations.

Open Access This article is licensed under a Creative Commons Attribution-NonCommercial-NoDerivatives 4.0 International License, which permits any non-commercial use, sharing, distribution and reproduction in any medium or format, as long as you give appropriate credit to the original author(s) and the source, provide a link to the Creative Commons licence, and indicate if you modified the licensed material. You do not have permission under this licence to share adapted material derived from this article or parts of it. The images or other third party material in this article are included in the article's Creative Commons licence, unless indicated otherwise in a credit line to the material. If material is not included in the article's Creative Commons licence and your intended use is not permitted by statutory regulation or exceeds the permitted use, you will need to obtain permission directly from the copyright holder. To view a copy of this licence, visit http://creativecommons.org/licenses/by-nc-nd/4.0/.

© The Author(s) 2025